JOURNAL OF GEOPHYSICAL RESEARCH, VOL. 104, NO. B1, PAGES 1077–1093, JANUARY 10, 1999

Kinematics of the India-Eurasia collision zone from GPS measurements

Kristine M. Larson,[1,2] Roland Bürgmann,[3] Roger Bilham,[4] and Jeffrey T. Freymueller[5]

Abstract. We use geodetic techniques to study the India-Eurasia collision zone. Six years of GPS data constrain maximum surface contraction rates across the Nepal Himalaya to 18 ± 2 mm/yr at 12°N ±13° (1σ). These surface rates across the 150-km-wide deforming zone are well fitted with a dislocation model of a buried north dipping detachment fault striking 105°, which aseismically slips at a rate of 20 ± 1 mm/yr, our preferred estimate for the India-to-southern-Tibet convergence rate. This is in good agreement with various geologic predictions of 18 ± 7 mm/yr for the Himalaya. A better fit can be achieved with a two-fault model, where the western and eastern faults strike 112° and 101°, respectively, in approximate parallelism with the Himalayan arc and a seismicity lineament. We find eastward directed extension of 11 ± 3 mm/yr between northwestern Nepal Lhasa, also in good agreement with geologic and seismic studies across the southern Tibetan plateau. Continuous GPS sites are used to further constrain the style and rates of deformation throughout the collision zone. Sites in India, Uzbekistan, and Russia agree within error with plate model prediction.

1. Introduction

While the far-field plate motions across the India-Eurasia collision zone are relatively well understood, the plate boundary encompasses a large area, the details of the deformation field are complicated, and geologic rates are poorly known (see Figure 1). Global plate motion models [*DeMets et al.*, 1990; 1994] predict that approximately 50 mm/yr of northward directed convergence is taken up between India and Eurasia. Geologic and seismic evidence suggests that 18±7 mm/yr of the convergence is expressed as shortening across the Himalaya [*Molnar and Deng*, 1984; *Armijo et al.*, 1986; *Molnar and Lyon-Caen*, 1989]. This means that nearly two thirds of the convergence is accommodated elsewhere.

Two competing mechanisms can describe this accommodation. It is clear that some of the India-Eurasia collision is accommodated by strike-slip faulting in Asia [*Molnar and Tapponnier*, 1975], with corresponding eastward displacement or extrusion of Tibet and southern China. Convergence also clearly leads to crustal thickening evidenced in the ~5 km average elevation of the Tibetan plateau and a crustal thickness of ~70 km. The relative importance of these two mechanisms, crustal thickening and lateral extrusion, is still a question of open debate. Estimates of convergence accommodated by extrusional tectonics range from 15% [*England and Molnar*, 1997a], to 10–25% [*Molnar et al.*, 1987], and up to 50% [*Avouac and Tapponnier*, 1993]. Unfortunately, geologic measurements across the major strike-slip and normal faults in the region, which would bound lateral extrusion, are fairly uncertain [e.g., *Molnar et al.*, 1987; *Avouac and Tapponnier*, 1993; *England and Molnar*, 1997a]. Resolving the crustal thickening versus lateral extrusion debate has important consequences for geodynamic models of the region [e.g., *England and Houseman*, 1986; *Avouac and Tapponnier*, 1993; *Houseman and England*, 1993; *England and Molnar*, 1997b; *Royden et al.*, 1997].

Many of these debates would be resolved if precise measurements of surface deformation throughout the plate boundary region were available. Currently available kinematic descriptions of the deformation field have been based on either seismic or geologic data [*Peltzer and Saucier*, 1996; *Avouac and Tapponnier*, 1993; *England and Molnar*, 1997a; *Holt et al.*, 1995]. While seismic and geologic data directly relate to deformation at the Earth's surface, both are hampered by large uncertainties. Furthermore, seismic observations

[1]Department of Aerospace Engineering Sciences, University of Colorado, Boulder.

[2]Now at Department of Geophysics, Stanford University, Stanford, California.

[3]Department of Geology and Geophysics, University of California, Berkeley.

[4]Department of Geological Sciences and Cooperative Institute for Research in Environmental Sciences, University of Colorado, Boulder.

[5]Geophysical Institute, University of Alaska, Fairbanks.

Paper number 1998JB900043.
0148-0227/99/1998JB900043$09.00

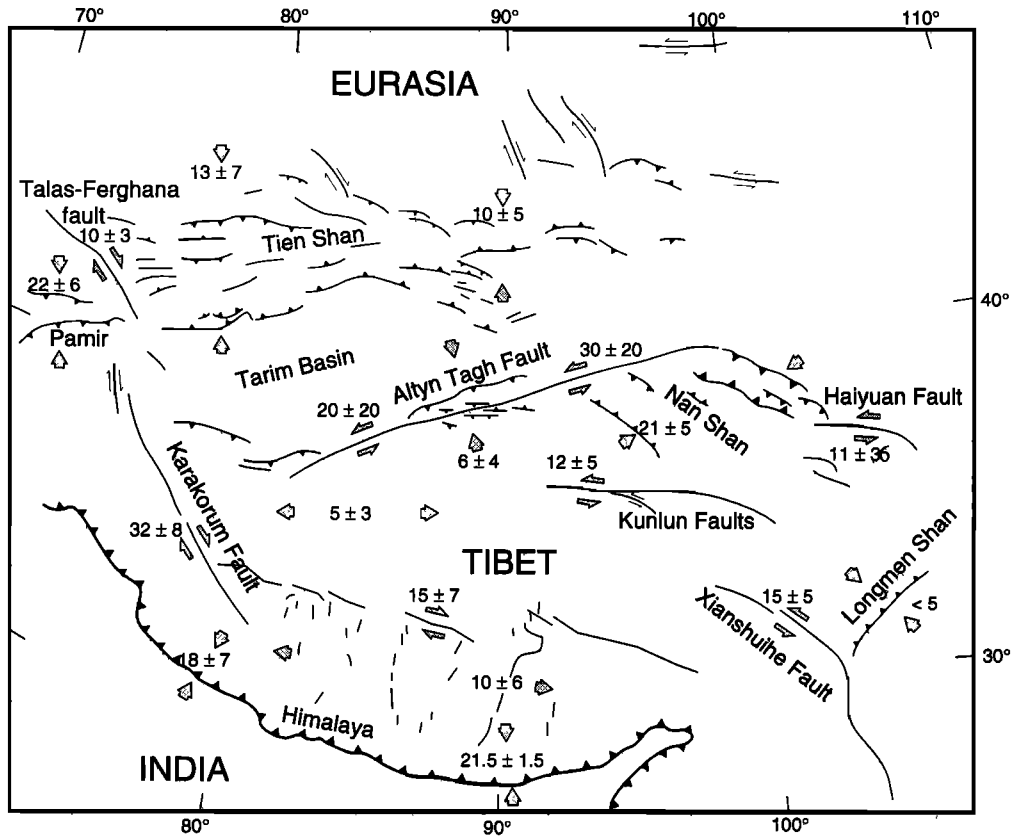

Figure 1. Tectonic setting and fault map of the India-Eurasia collision zone. Also shown are major collisional belts and fault zones with estimates of strike-slip or convergence rates (all in mm/yr). These rates and their standard deviations are determined from a variety of geologic data such as offset lithologic, structural, or morphologic units and cross-section restorations that span variable time periods. Geologic evidence suggests that 18±7 mm/yr of arc-perpendicular shortening is accommodated across the Himalaya and 10±5 mm/yr of east-west extension is accommodated across southern Tibet. Source references are as follows: Tien Shan, *Molnar and Deng* [1984]; Talas-Ferghana, *Burtman et al.* [1996]; Himalaya, *Molnar* [1987] and Lavé and Avouac (submitted manuscript, 1998); Northern Tibet grabens, *England and Molnar* [1997b]; Southern Tibet grabens, *Armijo et al.* [1986]; Karakorum, *Avouac and Tapponnier* [1993]; Karakorum-Jiali, *Armijo et al.* [1989]; Altyn Tagh, *Avouac and Tapponnier* [1993] and *Peltzer et al.* [1989]; North Pamir, Haiyuan, Nan Shan, and Kunlun, *England and Molnar* [1997b]; Longmen Shan, *Burchfiel et al.* [1996].

span a time too short to be representative of the regional kinematics, whereas geologic data may include features that are not representative of the currently active system. Geodynamic models that rely on these less precise constraints are limited in their ability to correctly interpret the kinematics of crustal deformation in the region. Geodesy provides the most accurate means of measuring surface deformation, but the observed rates are valid only during the short measurement period. That is, near plate boundary faults (such as the southern Himalaya thrust system) we commonly capture the interseismic deformation stage in the local earthquake cycle, whereas away from plate boundaries, geodetic data often agree well with long-term geologic displacement rates.

We use Global Positioning System (GPS) measurements to address the geodynamics of the India-Eurasia collision at two scales. A dense network across and along the Nepal Himalaya reveals details of the accommodation of interseismic strain where the Indian plate underthrusts the southern Tibetan plateau. Data from the Nepal Himalaya network together with seven regional continuous GPS stations quantify the magnitude of shortening that occurs north of the Himalaya and reveal eastward extrusion of southern Tibet. Finally, consideration of all currently available geodetic constraints on the regional kinematics allows us to compare and contrast active surface deformation with previously proposed models of the geodynamics of the collision zone.

The Nepal Himalaya embrace the central third of the Himalayan arc, including the rupture zones of the 1934 Bihar earthquake (M_w =8.1) and the 1833 Nepal earthquake (M ~7.7) [*Khattri*, 1987; *Bilham*, 1995]. The current slip potential of western Nepal and the Kumaon Himalaya (to the west of Nepal) is believed to be 6–15 m based on measured convergence rates and the absence of great earthquakes for at least the past 300 years of colonial history, which would be sufficient to drive a

magnitude M_w 8.1–8.7 earthquake [*Bilham et al.*, 1995; *Khattri*, 1987]. Geodynamically, these observations are important because they offer a view of convergent plate processes both in the hanging wall and in the footwall of a megathrust, a view that is obscured by oceans for most convergent plate boundaries.

Our current work builds on previous analyses of geodetic data from the Nepal Himalaya. Studies of leveling data from eastern Nepal reveal a peak uplift rate of 5–8 mm/yr which can be interpreted as interseismic strain accumulation associated with slip deceleration at a crustal ramp [*Jackson and Bilham*, 1994; *Pandey et al.*, 1995]. *Freymueller et al.* [1996] took a larger perspective and analyzed GPS data from one site in India and one site in Nepal to confirm global predictions of Indian plate motion independent of the Australian plate [*DeMets et al.*, 1990]. *Bilham et al.* [1997] presented an analysis and interpretation of GPS data collected in the Nepal Himalaya over a 4.5 year period. They found a 17±2 mm/yr northerly directed surface convergence rate between India and southernmost Tibet. Eighty percent of this convergence is concentrated in a zone less than 120 km wide.

Bilham et al. [1997] also used a 20 year time series of leveling data across the peak uplift zone. The center and maximum gradient of the horizontal velocity field is associated with the region of rapid uplift. The narrow width of the horizontal and vertical velocity fields is consistent with a two- dimensional dislocation model in which the Indian plate is locked to the base of the Himalaya down to depths of 15±5 km, north of which the Indian plate slides freely beneath the Tibetan plateau at a rate of 20±3 mm/yr.

In this paper we use more recently collected GPS data to improve relative velocity estimates in the Nepal Himalaya and have extended this local network with sites that were not previously available. One new site in particular, Lhasa, allows us to measure east-west extension rates across southern Tibet. We use the GPS and leveling observations in the Himalaya to invert for the geometry and slip rates of three-dimensional dislocation models representing interseismic strain accumulation. In particular, we focus on implications of significant along-arc variations in the present strain field. We have simultaneously analyzed data for the local network with data from continuously operating GPS sites in Asia and have defined all velocities in a consistent reference frame. This approach allows us to describe the kinematics of the India-Eurasia collision zone over a much broader scale. Finally, we include published present-day geodetic results from Asia in order to provide the reader with a more comprehensive description of the plate boundary deformation.

2. GPS Network and Observation History

The GPS data used in this study were collected between 1991 and 1997, mostly in campaign style measurements lasting from 3 to 5 days. Thirty sites in the plate boundary region are included in our analysis. Nearly all the Nepalese sites were first observed in 1991. Measurements were first made at Bangalore in 1991 (in a noncontinuous mode); all the other far-field stations began continuous observations about 1995, as did Lhasa. Locations of the sites in the Nepal Himalaya and Tibet network are shown in Plate 1 on a shaded relief map of the topography. Our sites span a considerable range in ellipsoidal heights, from less than 50 m in the foothills of the Himalaya to more than 7800 m on the South Col of Mount Everest. To provide additional tectonic background for the network, Plate 1 also includes maximum principal stress orientations [*Zoback*, 1992] and selected focal mechanisms [*Molnar and Lyon-Caen*, 1989].

The locations of all the sites used in this study are listed in Table 1, along with the number of observations at each site and their temporal span. The first GPS observations of the Nepal Himalaya network were made in April 1991. At this time the GPS constellation consisted of only 15 satellites, ambiguity resolution was difficult, and the global GPS tracking network was significantly smaller than the one available in 1997. The impact on the quality of geodetic results in the Himalaya is straightforward: the precision of each day's measurements in the east and vertical components is markedly poorer than what we observe for data collected in later years. For example, the standard deviations for 5 days of measurements made in 1991 were 2, 8, and 20 mm in the north, east, and vertical components for the 70 km baseline between JIRI and NAGA. In 1995 the values were 2, 2, and 10 mm, respectively. The 1991 results were negatively affected by the receivers available at the time, primarily C/A code L1/ squaring L2 receivers (Trimble SST). The WM-102 receivers used at TING and RONG observed for shorter time periods with more frequent phase breaks than those of the Trimble SSTs, resulting in east components for TING and RONG much weaker than those for the other sites. We could not resolve carrier phase ambiguities using either the Trimble SST or WM-102 data. In 1992 a subset of six sites was observed for 2 days. A second major experiment was conducted in November 1995. These measurements were conducted in collaboration with Project Idylhim [*Bilham et al.*, 1997]. Carrier phase ambiguities were easily resolved for the 1995 Nepalese data.

Several of the original Nepal Himalaya sites were not observed in 1995, including PHER, NAMC, KHAN, LUKL, SIMA, and MAHE. We were able to reoccupy most of these sites over the next year. In fall 1996 and spring 1997 we made additional measurements at NAGA, SIMI, BIRA, and NEPA. We have also included measurements collected in 1995 and 1997 from the South Col (SCOL) of Mount Everest by another group of scientists. The analysis thus includes GPS data from January 1991 through September 1997.

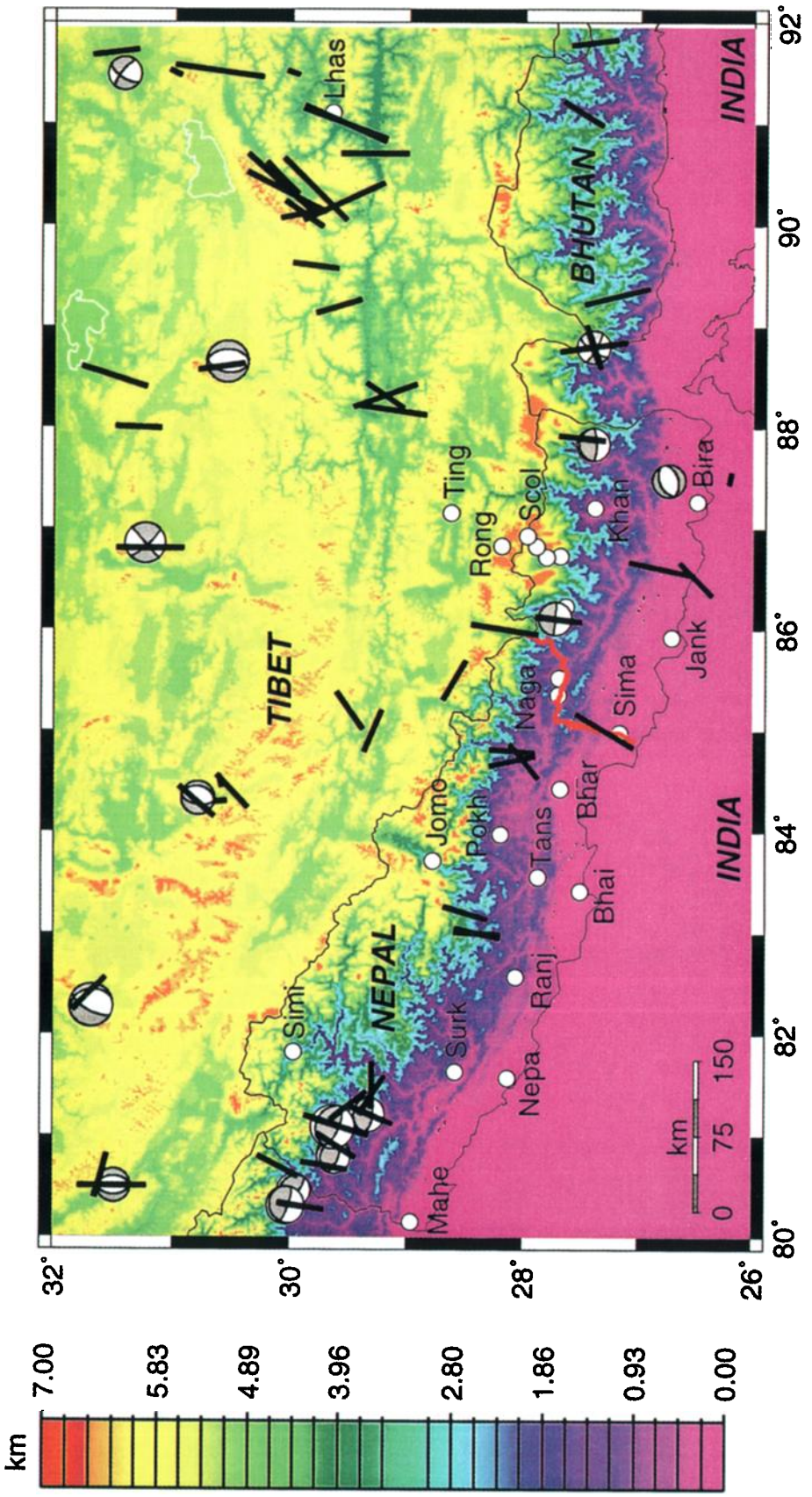

Plate 1. Close-up view of the Nepal Himalaya GPS network (open circles) plotted on a shaded relief map of the topography. The network spans over 7800 m in elevation and extends over 700 km along the Himalaya. Also shown are maximum principal stress orientations (scaled by the quality of the data point) in black [*Zoback*, 1992] and selected focal mechanisms [*Molnar and Lyon-Caen*, 1989]. The eastern Nepal leveling line discussed by *Jackson and Bilham* [1994] and *Bilham et al.* [1997] is shown as a thick red line. Regional country boundaries are also shown. Station names are defined in Table 1. Southwest from SCOL are the stations PHER, NAMC, and LUKL.

Table 1. GPS Sites Used in This Study

No.	Name	Identifier	Latitude deg	Longitude deg	Height m	Observing Sessions First	Last	Total	Epochs
1	Airport	AIRP	27.69715	85.35791	1283.848	1991.23	1995.87	10	2
2	Bhairhawa	BHAI	27.50734	83.41802	41.430	1991.25	1995.87	8	3
3	Bharatpur	BHAR	27.67783	84.42958	149.762	1991.25	1995.87	11	2
4	Biratnagar	BIRA	26.48396	87.26440	13.624	1991.23	1996.97	15	5
5	Bangalore	IISC	13.02116	77.57036	842.198	1991.08	1997.73	95	37
6	Irktusk	IRKT	52.21902	104.31623	502.449	1995.75	1997.73	33	12
7	Janakpur	JANK	26.71064	85.92452	7.249	1991.23	1995.89	8	2
8	Jiri	JIRI	27.63541	86.23035	1878.205	1991.23	1995.89	15	4
9	Jomoson	JOMO	28.78069	83.71787	2806.276	1991.23	1995.90	28	5
10	Khadbari	KHAN	27.37987	87.20560	1088.499	1991.25	1996.29	11	2
11	Kitab	KIT3	39.13476	66.88544	622.599	1994.80	1997.73	82	41
12	Lhasa	LHAS	29.65733	91.10398	3624.677	1995.38	1997.73	89	30
13	Lukla	LUKL	27.68333	86.72500	2768.700	1991.24	1996.95	4	2
14	Mahendre.	MAHE	28.96319	80.14795	161.000	1991.27	1996.79	7	3
15	Nagarkot	NAGA	27.69271	85.52121	2105.150	1991.10	1997.28	95	30
16	Namche	NAMC	27.80262	86.71514	3522.882	1991.25	1996.31	12	4
17	Nepalganj	NEPA	28.13409	81.57467	89.214	1991.23	1996.86	16	6
18	Pheriche	PHER	27.89373	86.82282	4361.658	1991.27	1997.28	7	2
19	Pokhara	POKH	28.19895	83.97768	767.763	1991.27	1995.87	10	3
20	Bishkek	POL2	42.67976	74.69426	1714.199	1995.40	1997.73	43	19
21	Ranj	RANJ	28.06254	82.57303	1654.130	1991.27	1995.88	8	2
22	Rongbok	RONG	28.19370	86.82739	4953.110	1991.25	1995.86	5	2
23	South Col	SCOL	27.97294	86.92943	7861.972	1995.36	1997.39	3	2
24	Shanghai	SHAO	31.09964	121.20044	22.142	1995.06	1997.39	86	38
25	Simara	SIMA	27.16245	84.98172	68.433	1991.25	1996.97	10	4
26	Simikot	SIMI	29.96698	81.82646	2908.145	1991.25	1996.86	13	4
27	Surkhet	SURK	28.58576	81.63519	626.803	1991.27	1995.89	14	4
28	Taipei	TAIW	25.02133	121.53654	43.945	1992.37	1997.73	215	97
29	Tansen	TANS	27.87384	83.55380	1391.444	1991.25	1995.90	10	4
30	Tingri	TING	28.62950	87.15521	4256.033	1991.25	1995.86	9	2

Latitudes, longitudes, and heights are referenced to the WGS84 ellipsoid. Each observing session consists of one 24-hour period. Epochs are defined as the number of distinct 2-week periods during which at least one observing session occurred.

3. GPS Data Analysis

The GPS data are analyzed with the use of the GIPSY software developed at the Jet Propulsion Laboratory [*Lichten and Border*, 1987]. We use an analysis strategy discussed fully by *Larson et al.* [1997]. In short, regional observations from each 24-hour period are analyzed simultaneously with data from the GPS global tracking network. In addition to site coordinates, we explicitly estimate initial conditions for each satellite, satellite and receiver clocks, solar radiation pressure parameters, a tropospheric zenith delay parameter for each site, and carrier phase ambiguities. Station coordinates and covariances from each 24-hour solution are then used in a weighted least squares fit, where the motion of each site is allowed to vary linearly. We use 51 sites in our global velocity determination but discuss only those in the Eurasia-India collision zone. The velocities of sites in western Europe, South America, the Pacific, Antarctica, Australia, and North America agree well with the results of *Larson et al.* [1997]. The scale, translation, and rotation of the epoch positions and velocities are constrained to agree with ITRF94 in a weighted least squares sense [*Boucher et al.*, 1996]. The resulting horizontal and vertical velocities of each site in the region are listed in Table 2.

4. Kinematics of the Collision Zone

4.1. Regional Plate Motions and Plate Boundary Deformation Zone

To address the far-field plate motions in the region, we compare the GPS-derived velocities with global plate model predictions of the No-Net-Rotation NUVEL1-A model, hereafter NNR-A [*DeMets et al.*, 1990; 1994; *Argus and Gordon*, 1991]. NNR-A is a compilation of angular velocity vectors for 14 tectonic plates, including Eurasia and India. As these plate motion rates are constrained only by seafloor spreading data, there are

Table 2. Station Velocities

	GPS Observed			India NNR-A Prediction		Eurasia NNR-A Prediction	
Site	North	East	Up	North	East	North	East
AIRP	34.5 ± 1.5	38.1 ± 2.2	−5.2 ± 5.9	42.3	36.6	−5.0	25.1
BHAI	37.6 ± 1.6	38.8 ± 2.3	−3.3 ± 5.9	42.2	36.1	−4.5	25.1
BHAR	37.5 ± 1.6	36.4 ± 2.3	2.0 ± 5.9	42.3	36.3	−4.8	25.1
BIRA	38.8 ± 1.3	40.1 ± 1.9	−4.4 ± 4.6	42.4	37.7	−5.5	24.9
IISC	39.8 ± 1.2	42.2 ± 1.8	7.2 ± 3.0	41.5	40.1	−2.9	23.2
IRKT	−10.2 ± 3.1	26.3 ± 3.7	4.6 ± 5.7	41.2	34.6	−9.8	22.7
JANK	38.2 ± 1.6	39.1 ± 2.6	2.2 ± 6.6	42.4	37.2	−5.2	25.0
JIRI	29.9 ± 1.5	35.9 ± 2.2	2.4 ± 6.3	42.4	37.0	−5.3	25.0
JOMO	27.0 ± 1.5	35.8 ± 1.9	5.3 ± 4.1	42.2	35.6	−4.6	25.2
KHAN	32.8 ± 1.5	40.6 ± 2.2	6.6 ± 5.8	42.4	37.4	−5.5	25.0
KIT3	2.6 ± 2.0	28.5 ± 2.3	0.7 ± 3.1	38.9	23.0	0.2	26.0
LHAS	16.6 ± 2.5	44.2 ± 2.8	3.2 ± 3.9	42.5	37.9	−6.6	24.9
LUKL	28.3 ± 1.4	37.8 ± 2.3	1.9 ± 6.9	42.4	37.1	−5.4	25.0
MAHE	36.6 ± 1.4	33.2 ± 2.1	−2.3 ± 5.3	41.8	34.3	−3.6	25.3
NAMC	28.6 ± 1.5	39.7 ± 2.1	2.4 ± 5.5	42.4	37.1	−5.4	25.0
NAGA	35.2 ± 1.2	37.7 ± 1.6	1.1 ± 2.4	42.3	36.7	−5.1	25.1
NEPA	36.8 ± 1.3	35.1 ± 2.0	−2.6 ± 4.6	42.0	35.1	−4.0	25.2
PHER	27.1 ± 1.3	37.3 ± 2.1	7.6 ± 5.1	42.4	37.1	−5.4	25.0
POKH	36.4 ± 1.6	36.9 ± 2.3	−7.0 ± 5.7	42.2	36.0	−4.6	25.2
POL2	3.7 ± 2.6	28.9 ± 3.0	9.3 ± 4.4	40.9	24.1	−2.0	25.8
RANJ	35.5 ± 1.6	32.3 ± 2.3	3.4 ± 6.1	42.1	35.5	−4.3	25.2
RONG	22.1 ± 2.6	36.4 ± 5.4	−18.6 ± 13.7	42.4	37.0	−5.4	25.1
SCOL	28.8 ± 3.6	39.7 ± 3.8	2.5 ± 17.9	42.5	37.1	−5.5	25.0
SHAO	−15.0 ± 2.2	31.8 ± 2.5	−2.5 ± 3.2	36.5	48.3	−13.3	22.2
SIMA	38.3 ± 1.4	35.7 ± 2.1	0.1 ± 5.7	42.3	36.7	−4.9	25.0
SIMI	24.2 ± 1.3	32.2 ± 2.0	9.0 ± 4.2	42.0	34.4	−4.0	25.4
SURK	35.8 ± 1.6	34.1 ± 2.3	1.5 ± 5.7	42.0	35.0	−4.0	25.3
TAIW	−13.6 ± 1.3	33.7 ± 1.4	−6.9 ± 1.7	36.4	48.5	−13.3	22.3
TANS	36.0 ± 1.5	35.4 ± 2.2	11.2 ± 5.6	42.2	35.9	−4.5	25.2
TING	21.4 ± 2.2	36.5 ± 4.2	−16.9 ± 8.7	42.4	36.9	−5.5	25.1

All velocities are in mm/yr. Uncertainties are 1 standard deviation. NNR-A, No-Net-Rotation NUVEL1-A model.

no direct data measuring the convergence rate between Eurasia and India.

In Table 2 we list the predicted NNR-A Eurasian and Indian plate velocity for each site adjacent to the observed velocities. Note that NNR-A predicts no vertical displacements. Depending on one's preferred vantage, station velocities can be depicted in an "India fixed" frame or a "Eurasia fixed" frame by subtracting the prediction for that plate. In Figure 2 we plot selected residual vectors to the Eurasian and Indian frames. Bangalore (IISC) and four sites in southern Nepal agree within 3 mm/yr with Indian plate motion predictions. Velocities of these sites relative to Eurasia range from 40±2 mm/yr toward N11°E at MAHE to 46±2 mm/yr toward N20°E at BIRA.

The remaining sites shown, including those in Kitab (KIT3), Taipei (TAIW), Shanghai (SHAO), Lhasa (LHAS), and Bishkek (POL2), are shown with respect to Eurasia. KIT3, IRKT, and POL2 do not show significant deformation with respect to Eurasia at the 95% confidence level, but their uncertainties are still quite large because the data span a short period of time. Shanghai's velocity with respect to Eurasia is 10±3 mm/yr toward N104°E. This is in good agreement with two independent analyses of VLBI data from Shanghai: *Heki* [1996] reported 11±1 mm/yr toward N112°E in a Eurasia fixed frame; *Molnar and Gipson* [1996] estimated 8±1 mm/yr toward N116°E, also in a Eurasia fixed frame. Taipei's velocity is rotated slightly with respect to Shanghai, 11±2 mm/yr east with respect to Eurasia. POL2, in the Tien Shan belt, has a velocity of 7±3 mm/yr toward N28°E with respect to Eurasia. If we take into account the large uncertainties in direction (±30°), this finding is in good agreement with an analysis by *Abdrakmatov et al.* [1996] (Figure 1b), which reported 5±3 mm/yr northward directed motion between POL2 and Eurasia.

We can also compare our analysis of data from LHAS with the recent work of *Kato et al.* [1998]. They report a Eurasia fixed velocity of 31±3 mm/yr toward N53°E±4°, which agrees well with our rate of 30±3 mm/yr toward N40°E±5°. The estimated directions disagree by 13°, but this variation is well within the 95% confidence region for the two estimates. Figure

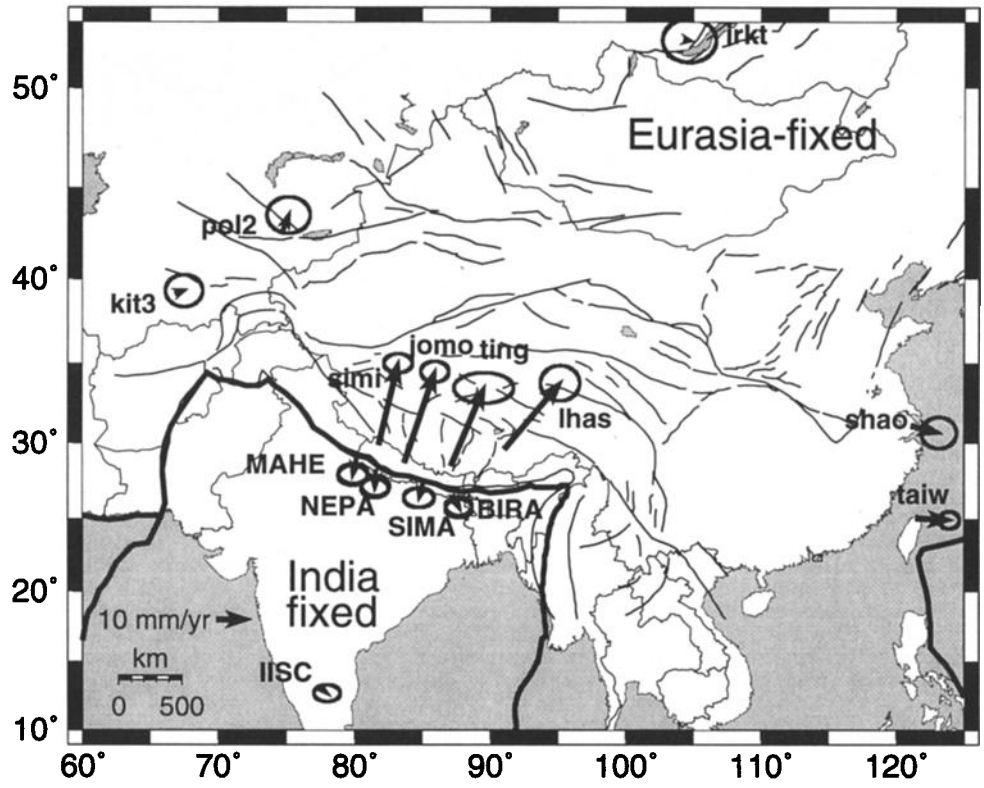

Figure 2. Regional velocities with 95% confidence ellipses shown in an India fixed frame (capitalized station names) or Eurasia fixed (lowercase station names) frame. The thick black line is the NUVEL1-A plate boundary between India and Eurasia.

2 shows that Lhasa's velocity is slightly rotated with respect to velocities from sites in northern Nepal. In Figure 3 we display selected velocity vectors with respect to Simikot (SIMI). This perspective demonstrates east-west extension of 11±3 mm/yr between SIMI and LHAS.

4.2. Himalayan Collision Zone

To look at the details of the Nepal Himalaya deformation, we plot velocities with respect to Nagarkot (NAGA) in Figure 4. This projection clearly shows that sites in southern Tibet (RONG and TING) are moving south with respect to NAGA and that sites in southern Nepal (e.g., BIRA and JANK) are moving north toward NAGA. Horizontal contraction across eastern Nepal (between BIRA and TING) is 18±2 mm/yr oriented N12°E±12° over 240 km. The situation is more complicated in western Nepal. While SIMI is moving southwest, as expected, sites in southwestern Nepal (MAHE and NEPA) are moving negligibly with respect to NAGA instead of northward as we see in eastern Nepal. This finding suggests that the zone of active contraction extends farther to the south in western Nepal. The velocity pattern in western Nepal is smooth, so our interpretation of a change in deformation pattern does not rely on a single station. The rate of shortening within the network in western Nepal (between SIMI, NEPA, and MAHE) is 13±2 mm/yr oriented N10°E±9° over 200 km, indicating a wider contraction zone than in east Nepal.

A change in convergence direction between eastern and western Nepal cannot be precisely determined from these data because of the large uncertainties in the estimated east components for many of the GPS stations. A rotation of the convergence direction would be consistent with earthquake focal mechanisms [*Molnar and Lyon-Caen*, 1989; *Ni and Barazangi*, 1984] and maximum principal stress orientations [*Zoback*, 1992], which also rotate counterclockwise from west to east along the arc to remain in an arc-perpendicular orientation, as shown in Plate 1. Arc-normal shortening is also consistent with east-west extension across southern Tibet [*Armijo et al.*, 1986].

Vertical velocity estimates derived from GPS are 2 to 3 times less certain than corresponding horizontal velocity estimates. Vertical velocities derived from campaign style GPS studies such as this one must be examined skeptically. Vertical accuracy is reduced by blunders in the measurement of true antenna height. Data analysts may misinterpret field notations of antenna height. Even so, we have not found a large number of outliers in the vertical estimates. Excluding TING and RONG, only six of the 22 Nepal Himalaya sites indicate significant velocities at the 1 standard deviation level (Table 2). The 1991 observations at TING and RONG are problematic because we used an antenna (WM-102) for

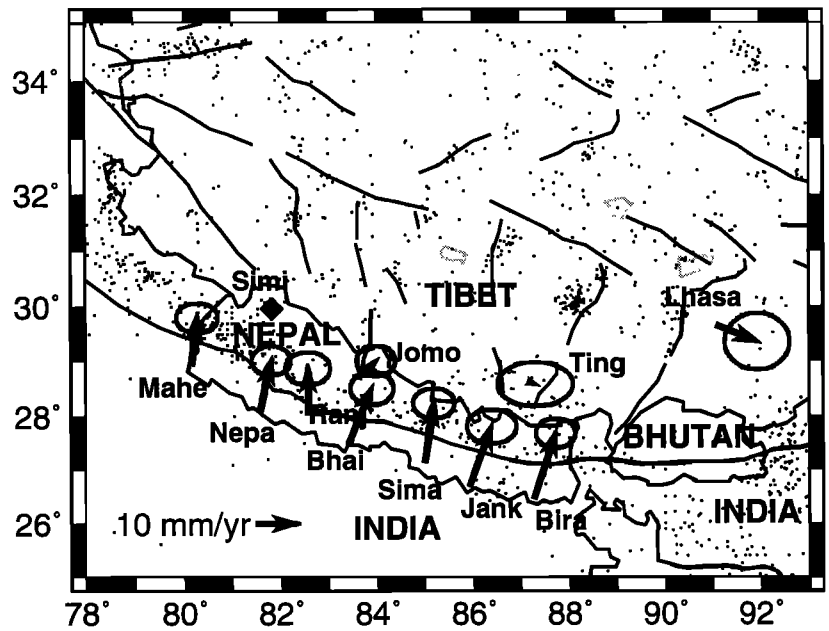

Figure 3. Selected regional velocities shown in relation to Simikot (diamond) with 95% confidence ellipses. Historic seismicity from 1950 to 1997 suggests a change in strike along the Himalaya at 83° longitude. India-Eurasia plate boundary and faults are shown in black.

which we have no calibration; we have therefore excluded these sites from further discussion. At one of the sites, AIRP, we have an independent measurement of the vertical velocity. Leveling data from the Kathmandu Valley (between NAGA and AIRP) measured subsidence of 7 mm/yr. This agrees with GPS vertical velocity estimates at AIRP of -6 ± 6 mm/yr.

5. Discussion

5.1. Interseismic Strain Accumulation Across the Himalaya

To better understand the process of strain accumulation in the Nepal Himalaya, we interpret GPS observations of surface deformation using three-dimensional dislocation models. The INDEPTH seismic reflection profile is located near 90° longitude and shows that a discrete fault plane dipping ~9° extends from 27.7° to about 29° latitude, where it reaches ~40 km depth [*Makovsky et al.*, 1996; *Zhao et al.*, 1993]. Deformation to the north of ~29° latitude below Tibet is likely to be accommodated by more widely distributed shear and asthenospheric flow in the lower crust and upper mantle. However, our data near the tip of the slipping Himalayan thrust system are quite insensitive to the rate, geometry, or mechanisms of deformation below Tibet. Therefore we postulate that the observed interseismic deformation is primarily caused by the aseismi-

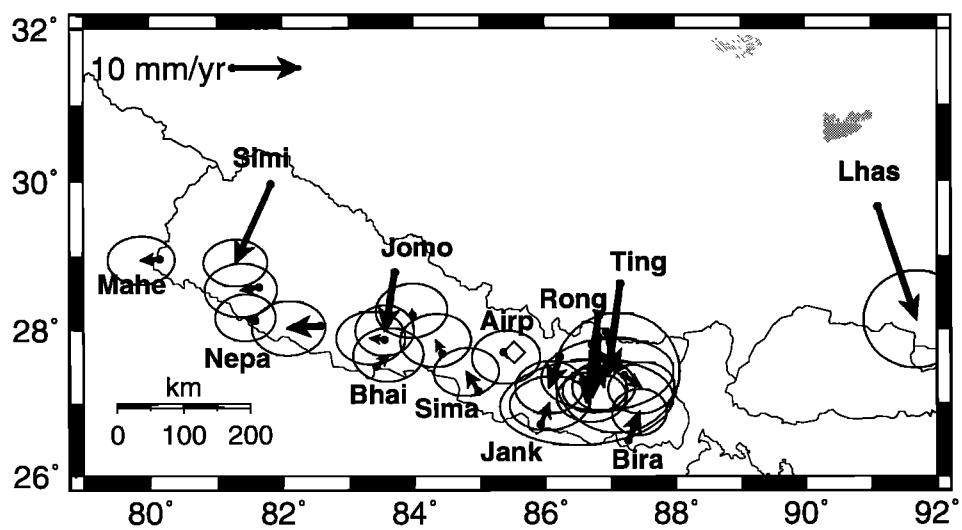

Figure 4. Regional velocities shown in relation to Nagarkot (diamond) with 95% confidence ellipses.

cally slipping portions of the thrust system below the Himalaya. The model faults reach far below Tibet to avoid edge effects from the northern tip of the finite dislocations. Our first-order models assume that the deformation can be characterized by slip on rectangular dislocation planes buried in a homogenous, isotropic and elastic half-space [*Okada*, 1985]. These dislocations represent aseismic shear north of the locked portion of the Himalayan detachment system.

Alternatively, interseismic deformation in underthrusting regimes can be modeled by the combination of steady block motion across the complete thrust surface with a dislocation that is slipping opposite to the thrust motion representing the locked portion of the fault [*Savage*, 1983; 1996]. Such a back-slip model implies that the actively slipping fault segments downdip of the back-slipping dislocation are parallel to the locked segment. For multiple sources of deformation that are not aligned we prefer modeling those active fault planes as finite width dislocations in an elastic half-space. We do not attempt here to model viscous relaxation processes expected to play a role in the crustal earthquake cycle, and we do not account for buoyancy effects. Data spanning many decades may eventually reveal unique evidence to differentiate such models from the elastic representations we utilize [*Thatcher*, 1986].

We use a constrained nonlinear optimization algorithm, which allows us to estimate the geometry (parameterized by length, depth, width, dip, strike, and location) and the rates of strike slip and dip slip of one or more faults that best fit the GPS and/or leveling data [*Arnadottir and Segall*, 1994; *Bürgmann et al.*, 1997]. Specifically, we seek models that minimize the weighted residual sum of squares, $\mathrm{WRSS} = (d_{\mathrm{obs}} - d_{\mathrm{mod}})^T P^{-1} (d_{\mathrm{obs}} - d_{\mathrm{mod}})$, where d_{obs} and d_{mod} are the observed and modeled velocity components, respectively, and P is the data covariance matrix. In some cases we apply bounds (such as constraints on the depth of faulting, the range of permissible fault strikes, or allowing for dip-slip faulting only) to find best fitting sources that are additionally constrained by geologic or other information. The model misfit is $\sqrt{\mathrm{WRSS}/(n-p)}$, where n is the number of data and p is the number of free model parameters. We compare our geodetic observations with relatively simple dislocation models to evaluate first-order characteristics of the collision zone revealed in the geodetic data. These models include a best fitting single fault plane and along-strike heterogeneity represented by two adjacent fault planes. We evaluated a wide range of additional models of varying complexity that led to the choice of models we show here. For example, we found that the data do not yet resolve significant down-dip variation in dip or slip magnitude of the active fault surface [*Bürgmann et al.*, 1997].

5.2. Model 1: Single Fault Plane

The simplest model of interseismic strain buildup across a dipping thrust fault consists of one dislocation with uniform slip located at the downdip tip of the locked fault. We solve for the best fitting single rectangular dislocation plane to represent aseismic fault slip north of the tip line of the locked system. The width and length of the fault plane are constrained to be 1000 km and 1500 km, respectively. The nonlinear inversion for nine fault parameters (geometry + dip slip and strike slip) of a single fault, with relatively wide bounds on the geometry, computes a dislocation striking 106°, dipping 4° to the north, following the southern edge of the Greater Himalaya at a depth of 18 km (Figure 5). We compute a dip-slip rate of 19±1 mm/yr and a strike-slip component of 4±1 mm/yr. The misfit of this model is 1.07; that is, the model provides an adequate fit to the data within the given uncertainties. Allowing only for dip slip, the fault strike rotates to 105°, and all other parameters change insignificantly, including a dip-slip rate of 20±1 mm/yr. If we invert only the GPS data, the model fault depth changes very little, to 19 km, and the fault dip increases to 8° with 20±1 mm/yr and 4±1 mm/yr of dip-slip and strike-slip, respectively. However, if we solve for dip slip only, the tip line deepens to 22 km, with 23±1 mm/yr of slip. Finally, if we fix the fault strike to 106° and invert only the leveling data, we compute a tip line depth of 14 km and a dip-slip rate of 15±2 mm/yr. The relative sensitivity to small variations in our model parameters suggests that the uncertainty in the detachment depth is ~3 km. Figure 5a shows the surface projections of the fault planes for the three cases we considered: only GPS data, both GPS and leveling data, and only leveling data, along with model and observed velocity vectors. In Figures 5b–5d we represent the velocity vectors in their fault parallel, fault perpendicular, and vertical components, along with the model predictions in these directions. All model parameters are listed in Table 3.

Overall, the leveling data appear to prefer a shallower and slower source of deformation. This preference could be caused by systematic errors in the data, may indicate differences in the deformation during the somewhat different time intervals covered by the GPS and leveling data, or may be related to insufficient consideration of the correlations in the leveling data [*Arnadottir et al.*, 1994]. The lack of slope dependent biases in the data [*Jackson and Bilham*, 1994], the consistency of the uplift pattern measured from 1977 to 1990 and from 1990 to 1995 along the northern 15 km of the level line, and inversion of the data with full consideration of the data covariances appear to rule out these causes. *Savage* [1998] shows that higher rigidities at depth lead to a systematic difference between inverted dislocation source depths of vertical and horizontal displacement data. For a horizontal detachment source placed in a half-space underlying a less rigid layer, leveling data would invert for a shallower and less rapidly slipping dislocation than would GPS data if we assume a homogeneous elastic half-space [*Savage*, 1998]. Thus the apparent shallowing of the inferred detachment source

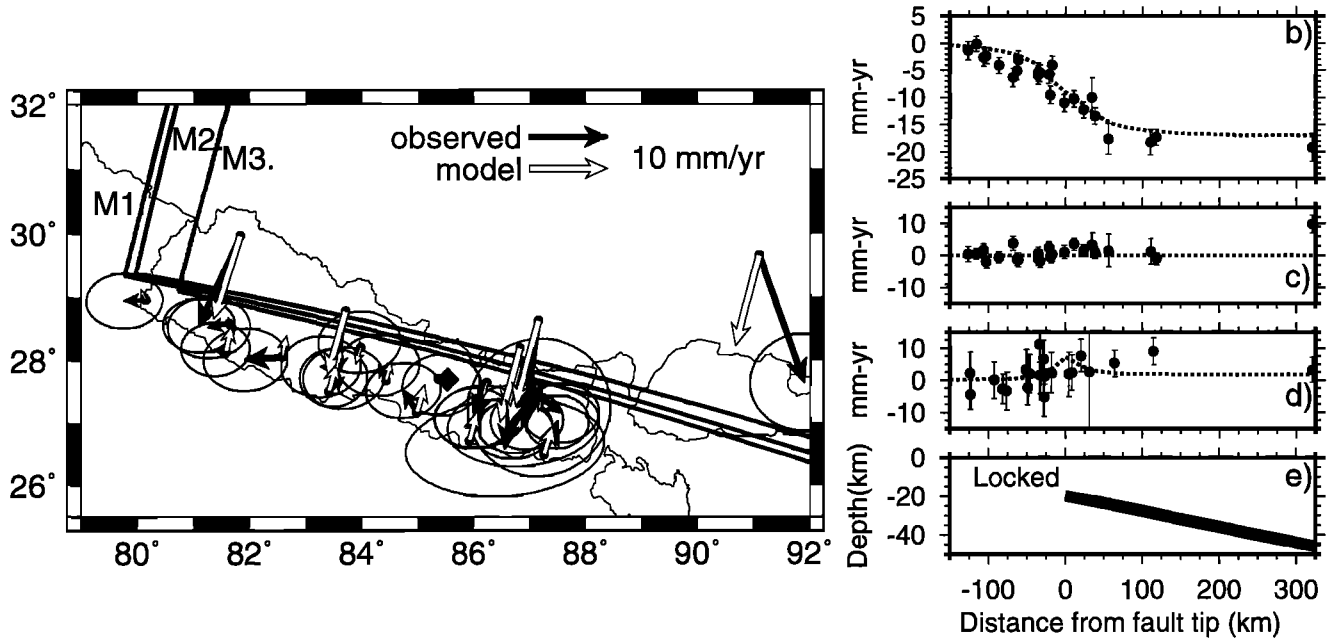

Figure 5. (a) Observed horizontal velocities relative to Nagarkot (solid vectors) and predicted horizontal velocities (open vectors) from best fit single fault plane model using both GPS and leveling data. Nagarkot is shown as a solid diamond. Uncertainties are 95% confidence ellipses. The surface projections of the fault plane using both GPS and leveling data (M1), only GPS data (M2), and only leveling data (M3) are shown in black. Also shown are the velocities of the GPS sites in (b) fault parallel (striking 105.3°), (c) fault perpendicular, and (d) vertical components, with 1 standard deviation uncertainties. M1 model predictions are shown as a dotted line in Figure 5b–5d. (e) Location of the locked zone in profile. Profiles in Figures 5b–5e are shown with respect to the distance from the fault tip. For further description of the fault model, see Table 3.

Table 3. Model Parameters

Fault	Data	Depth, km	Dip, deg	Strike, deg	Dip-slip, mm/yr	Strike-slip, mm/yr	Model Misfit
			Best Fitting One Fault Models				
Single	G+L	18.3	−4.4	106.4	−19.1 ± 10.9	3.6 ± 1.1	1.07
Single	G+L	17.6	−4.7	105.3	−19.6 ± 1.0	—	1.12
Single	G	18.7	−7.7	106.1	−20.1 ± 1.1	3.5 ± 1.2	1.23
Single	G	22.0	−9.7	104.4	−22.7 ± 1.2	—	1.32
Single	L	14.0	−14.8	106.1	−15.4 ± 1.6	—	0.93
			Best Fitting Two Fault Model				
West	G+L	25.0	−8.3	112.3	−23.4 ± 1.5	—	
East	G+L	14.6	−3.4	100.9	−20.8 ± 1.1	—	1.00
West	G	25.0	−8.4	112.3	−23.6 ± 1.6	—	
East	G	16.2	−2.3	99.4	−21.8 ± 1.3	—	1.06
			Two-Fault Model, Western Fault Aligned to Seismicity				
West	G+L	25.0	−4.5	120.0	−21.3 ± 1.6	4.3 ± 1.6	
East	G+L	14.9	−3.4	100.9	−19.6 ± 1.1	—	1.05
West	G	25.0	−4.5	120.0	−21.5 ± 1.6	4.2 ± 1.6	
East	G	16.2	−2.3	99.4	−19.4 ± 1.2	—	1.24

Data used are GPS (G) and/or leveling (L). Model misfit is defined in the text.

inverted from the leveling data may suggest layering of the Earth's crust with increasing rigidities at depth. Both horizontal and vertical deformation underestimate the source depth; that is, our inversion may be somewhat biased toward shallow depths. As the precision of geodetic data improves, we are increasingly sensitive to second-order details of our model parameterization including varying constitutive constants.

Other geologic and geophysical evidence supports our model based only on the geodetic data. The depth, dip, and location of the model fault plane agree quite well with the Main Himalayan Thrust reflector imaged by the INDEPTH seismic reflection experiment [*Makovsky et al.*, 1996; *Zhao et al.*, 1993]. The data confirm the existence of a relatively simple aseismically slipping detachment plane that accommodates most of the active India-Tibet convergence north of ~28° latitude. Instead of representing a simple dislocation slip plane, however, slip is probably accommodated in a narrow, strain-weakened shear zone, similar to mylonitic shears observed along thrust faults exhumed from midcrustal depth [e.g., *Ramsay*, 1980; *Kirby*, 1985; *Harrison et al.*, 1997].

Intermediate size earthquakes along the Himalayan arc consistently have focal mechanisms with a shallowly northward dipping nodal plane (Plate 1) and are thought to be events on the detachment system and associated secondary faults [*Baranowski et al.*, 1984; *Molnar*, 1990; *Ni and Barazangi*, 1984]. *Lavé and Avouac* (submitted manuscript, 1998) measured 21.5 ± 1.5 mm/yr of Holocene shortening across folds marking the southern tip of the Main Frontal Thrust in southern central Nepal. The agreement of these long-term contraction rates across the southern tip of the detachment system with the interseismic strain accumulation rates we measure at the base of the Greater Himalaya suggests that detachment slip efficiently accommodates most of the India-southern Tibet convergence. This lack of evidence for significant plastic strain north of the Main Frontal Thrust, the locked detachment south of the Greater Himalaya constrained by the geodetic data, and the insignificant contribution of moderate earthquakes to detachment slip indicate that most of this slip occurs in great Himalayan detachment earthquakes reaching from the southern Siwalik hills to the Greater Himalaya (Lavé and Avouac, submitted manuscript, 1998).

The single-dislocation model fits most of the data well within the uncertainties, the exceptions being sites in southwestern Nepal and LHAS. The model does not fit the data from LHAS within 95% confidence limits, but this fit is not to be expected, given that LHAS is affected by both extensional and contractional deformation. LHAS moves about 5 mm/yr faster southward than SIMI, showing that a small amount of north-south contraction may occur across the south Tibetan graben system. Removal of the LHAS data has little impact on model estimates. The single fault plane model does not predict the shift in displacement patterns along the southwestern edge of the network. As we move from eastern to western Nepal, the southernmost site velocities change from a small northward motion relative to NAGA to a more westerly trend with an insignificant north component. We therefore continue our investigation by allowing for a variation in fault geometry along the Himalaya.

5.3. Model 2: Two Adjacent Fault Planes

The western Nepal segment of the Himalayan thrust system has not experienced a significant earthquake for at least 300 years [*Bilham et al.*, 1997]. It is therefore important to evaluate whether this area behaves differently from the eastern region near Kathmandu, which is located in the hanging wall of the 1934 Bihar earthquake rupture. Variations could be due to the two regions being at different stages of the regional earthquake cycle or may stem from structural segmentation of the fault system. The seismicity band along the Himalaya experiences a sharp bend of about 20° to the northwest of 83° longitude, indicating a possible segment boundary near this longitude (Figure 3). We evaluate whether significant lateral variations are indicated by the data by modeling the deformation with two contiguous fault planes. In particular, we are interested in differences in the width of the locked fault plane, the depth to the fault, and variations in slip rate along the Himalayan range front. For this purpose we restrict the search to dip-slip on two faults that lie approximately adjacent to each other. Their absolute position, strike, dip, and depths are unconstrained.

We find significant variations in the depth of the two model faults. The tip of the eastern fault is at a depth of 15 km, but the western fault clearly prefers depths of 25 km or more. There is an apparent correlation between estimated slip magnitude and depth of faulting for the western fault. That is, within a certain range, deeper models with higher slip rates fit the data as well as the model at 25 km. We would be able to more confidently constrain the other fault parameters if additional constraints could be put on either the slip rate or the depth based on complementary data. The outline of the eastern and western faults, along with observed and predicted horizontal velocities, are shown in Figure 6a. Dip slip on the western and eastern fault segments are 23±2 mm/yr and 21±1 mm/yr, respectively. The two model fault planes rotate into approximate parallelism with the Himalayan arc (striking 112° and 101°, respectively). The western and eastern faults dip 8° and 3° to the north, respectively. The model misfit is reduced to 1.00. We evaluate the GPS data separately to examine the importance of the leveling data in this conclusion. We find that the resulting model is very comparable to the previous one, which used both GPS and leveling data (Table 3). The GPS data fit a two fault plane model significantly better than a one fault

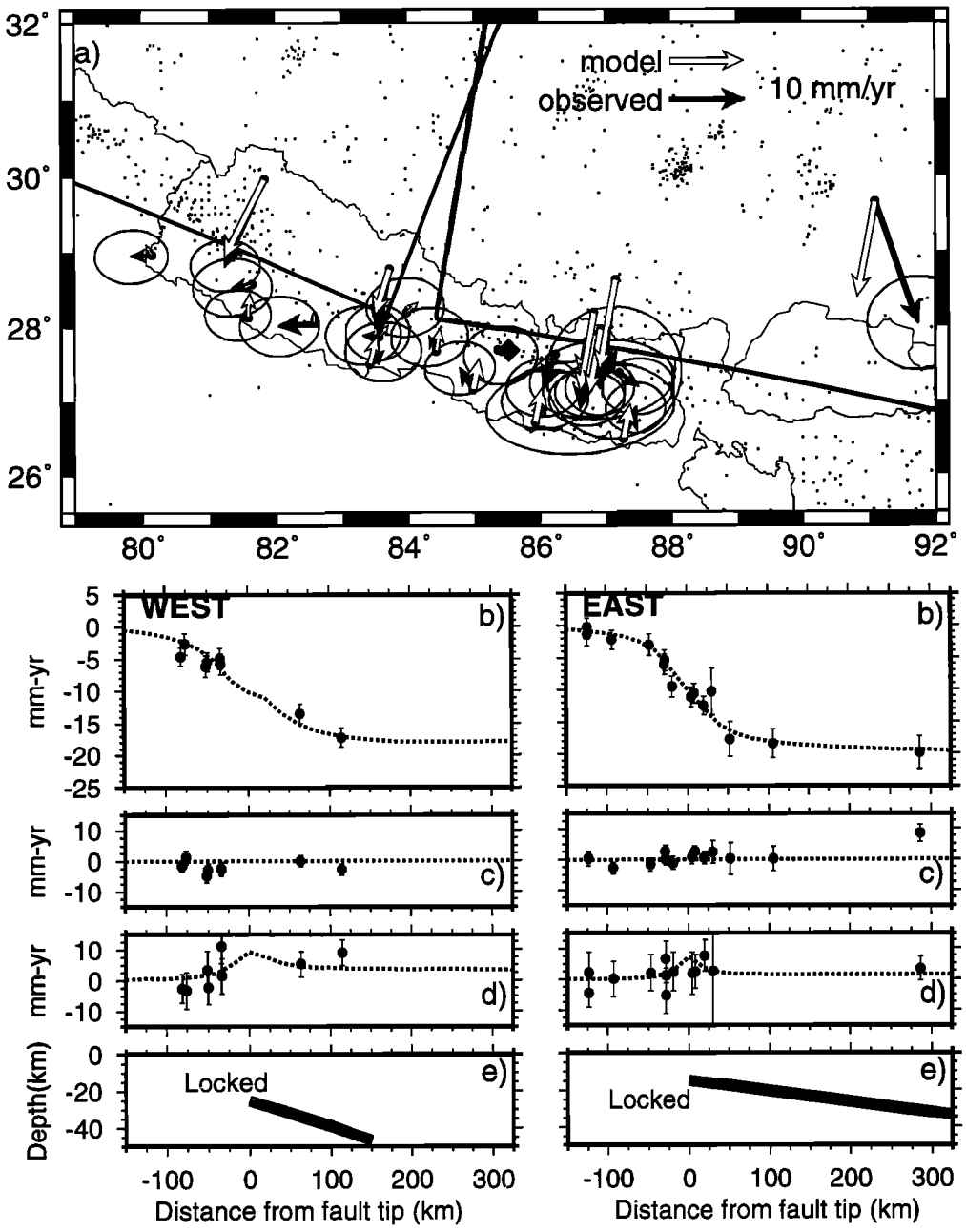

Figure 6. (a) Observed horizontal velocities relative to Nagarkot (solid vectors) and predicted horizontal velocities (open vectors) from best fit two fault plane model using both GPS and leveling data. Nagarkot is shown as a solid diamond. Uncertainties are 95% confidence ellipses. The surface projections of the fault planes using both GPS and leveling data are shown in black. Also shown are the velocities of the GPS sites in (b) fault parallel (striking 112.3° and 100.9°), (c) fault perpendicular, and (d) vertical components, with 1 standard deviation uncertainties. Model predictions for the western and eastern fault planes are shown as a dotted line in Figures 6b–6d. (e) Location of the locked zone in profile. Profiles in Figures 6b–6e are shown with respect to the distance from the fault tip. For further description of the fault model, see Table 3. Historic seismicity from 1950 to 1997 is also shown.

plane model, with a reduction in the model misfit from 1.32 to 1.06.

How well does this dislocation model fit the vertical GPS observations shown in Figure 6d? The WRSS for 22 site velocities improves from 18.6 to 11.8 when the model predictions are used instead of a null prediction. The improved fit suggests that some of the measured vertical GPS rates are in fact caused by the India-Eurasia collision, although because of the large uncertainties the vertical velocity estimates do not constrain the dislocation models.

The preferred "segment boundary" is near the rather

abrupt change in the strike of the seismicity near 83° longitude [*Tandukar et al.*, 1997]. It also coincides with the southern extension of the north-south striking Thakkhola graben southeast of Jomoson (JOMO), and a basement high (the Bundelkhand Massif and Faizabad Ridge) on the underthrusting Indian plate [*Khattri*, 1987]. This finding suggests that there may be a significant discontinuity between the western and eastern Nepal deformation zone, along what is otherwise a smooth small-circle arc of high elevations, topographic roughness, and seismicity [*Bilham et al.*, 1997; *Seeber and Gornitz*, 1983]. Interaction of the underthrusting basement high with the overriding plate may be the cause for this observed lateral heterogeneity.

Notwithstanding this apparent relation between western Nepal seismicity and inferred deformation kinematics, we note that the geometry of the western 112° striking model fault plane does not exactly follow the observed seismicity band striking 120°. We have therefore tested another two-fault model in which we force the western model thrust to more closely follow the 120° striking seismicity band (Table 3). Allowing only dip-slip deformation, we cannot fit the data for SIMI and JOMO, with a correspondingly large model misfit of 1.30. If we allow strike slip as well as dip slip, we have a good fit to the observations, with a misfit of 1.05, compared to 1.00 for the best fitting two fault plane model with dip slip only. This model implies that about 4 mm/yr of right-lateral strike slip is accommodated across western Nepal. Mapped right-lateral strike-slip faults striking ESE through western Nepal [*Upreti*, 1996] presumably respond to this inferred dextral shear.

As we noted above, the differences between motions in western and eastern Nepal could also be due to these regions being in different stages of the earthquake cycle. Preliminary layered viscoelastic models that consider the possible effects of continued postseismic relaxation from the 1934 Bihar earthquake (F. Pollitz and R. Bürgmann, unpublished models, 1998) predict up to 5 mm/yr of transient northward motion and localized contraction and uplift in eastern Nepal, somewhat consistent with the observed difference between western and eastern Nepal motions. This gravitational relaxation model includes a viscous lower crust from 25 to 40 km depth (with viscosity $\nu = 10^{19}$ Pa s), has increasing shear and bulk moduli with depth, and accounts for gravitational effects [*Pollitz*, 1997]. If we remove the modeled contribution of viscous relaxation of the 1934 Bihar earthquake from the observed GPS velocities and invert once more for the best fitting two-fault dislocation model, we find that the inverted depth of the eastern fault plane deepens to greater than 20 km. That is, instead of being related to a structural heterogeneity along the Himalayan arc, the lateral variations of the displacement field may reflect residual effects of a large earthquake 60 years ago that is superimposed on the secular aseismic fault slip. However, data spanning longer time periods will be needed to uniquely resolve the contribution of viscous and gravitational processes to the observed surface deformation.

5.4. Kinematics of the India-Eurasia Collision Zone

Our analysis has focused on the Himalayan frontal thrust and southern Tibet but also includes more distributed, continuously operating sites in the India-Eurasia collision zone. Additional published results are available for some areas in central and east Asia. Even without a formal combination of the networks we can continue our discussion by evaluating existing geodetic constraints in the broader context of the kinematics of the India-Eurasia collision. In Figure 7 we show shortening, extension, and strike-slip rate estimates from published geodetic studies [*Abdrakmatov et al.*, 1996; *Kato et al.*, 1998; *King et al.*, 1997; *Michel et al.*, 1997; *Royden et al.*, 1997] and our own results together with selected station velocities referenced to Eurasian plate motion. While many questions pertaining to the kinematics of the collision zone remain unanswered, we can address three regional issues including (1) the northern limit of the broader India-Eurasia collision zone, (2) east-west extension in southern Tibet, and (3) the extent of eastward motion of south China. A number of geodetic experiments are in progress that will eventually resolve many of the remaining unanswered questions of how plate boundary strain is distributed in this region.

Continuous sites KIT3 (3±2 mm/yr) and IRKT (4±2 mm/yr) and the station AZOK (2±3 mm/yr) reported by *Abdrakhmatov et al.* [1996] have insignificant velocities at the 95% confidence limit in relation to the Eurasian plate. This finding shows that only a minimal amount of plate boundary strain may exist northwest of the Pamirs and north of the Tien Shan and Mongolia, consistent with seismologic and geologic estimates [*England and Molnar*, 1997b]. The broad distribution of north-south shortening across the India-Eurasia collision zone is best resolved in the west. Results from the Pamirs [*Michel et al.*, 1997; G. Michel, personal commununication, 1998], the Tien Shan [*Michel et al.*, 1997; *Abdrakmatov et al.*, 1996], and our measurements from western Nepal fully account for the convergence between India and Eurasia, with observations of 50±6 mm/yr compared with model predictions of 44 mm/yr. This finding suggests that Himalayan shortening across northwest India and Kashmir, located south of the Pamirs, is comparable to that observed across the Nepal Himalaya to the east. Even so, the uncertainties are quite high, and determination of how strain is partitioned in detail and what role rotating blocks and strike-slip faults may play will require additional measurements, denser station spacing, and formal integration of the individual networks.

In addition to contraction across the Himalaya, we measure east-west extension in southern Tibet of 11±3

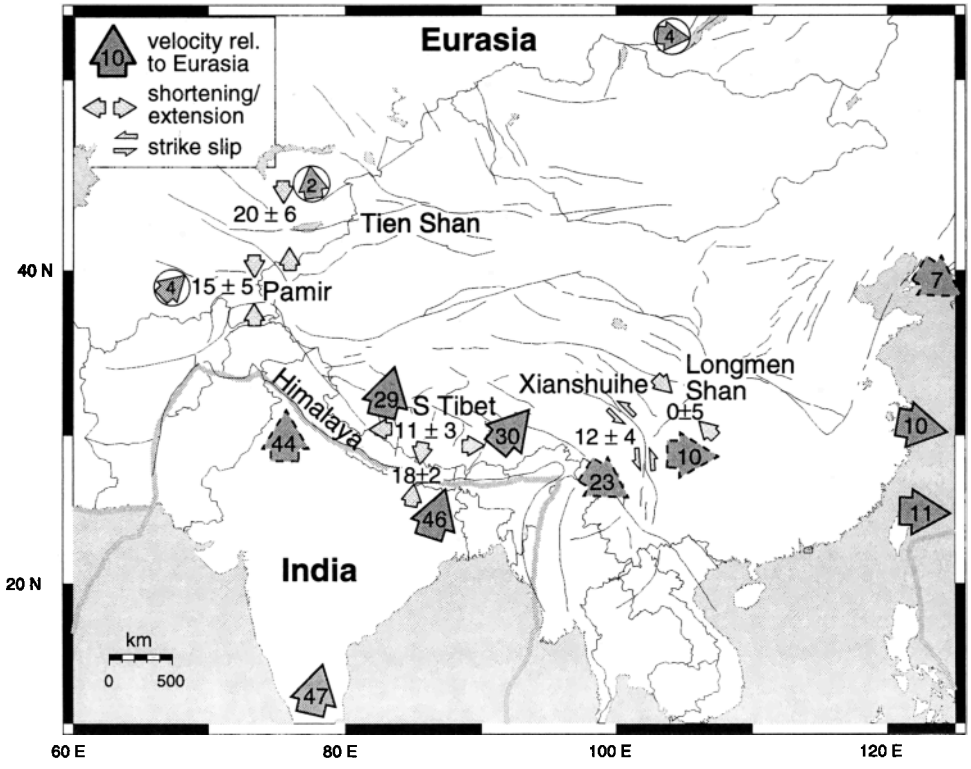

Figure 7. Summary of geodetically determined deformation rates across the India-Eurasia collision zone integrating our results with published studies. Large solid arrows indicate velocities relative to Eurasia from this study. Arrows with dashed outline are sites from other publications such as Taejeon on the Korean Peninsula [*Kato et al.*, 1998] and Azok in the northernmost Tien Shan [*Abdrakhmatov et al.*, 1996] or are inferred assuming a rigid south China block (east and west of Xianshuihe fault) and Indian subcontinent (northwest India). Arrows in circles are used to show velocities that show no significant motion with respect to Eurasia at the 95% confidence limit. Small gray arrows show active deformation rates determined from several years of GPS measurements across the Tien Shan [*Abdrakhmatov et al.*, 1996], the northern Pamir and western Tien Shan [*Michel et al.*, 1997; G. Michel, personal communication, 1998]; the Himalaya [*Bilham et al.*, 1997; this study], the Xianshuihe fault [*King et al.*, 1997; *Royden et al.*, 1997], and the Longmen Shan [*King et al.*, 1997]. Shortening across the Indian subcontinent south of the Himalaya (not shown) is constrained to be less than 2 mm/yr [*Paul et al.*, 1995; *Bilham et al.*, 1995].

mm/yr between SIMI and LHAS, which is consistent with geologic and seismic reports for the region. The rate of extension across southern Tibet has been estimated as 5–10 mm/yr from seismic moment release in earthquakes [*Baranowski et al.*, 1984] and 10±5 mm/yr from extensive geologic mapping and Landsat image interpretation [*Armijo et al.*, 1986]. On the basis of geometric considerations of arc-normal thrusting of Tibet over the Indian plate, *Molnar and Lyon-Caen* [1989] estimate extension rates of 18±9 mm/yr and ~10 mm/yr in southern and central/northern Tibet, respectively. As they included the full arc width from 75° to 95° longitude, this higher value is consistent with our estimate. Using similar geometric arguments, *Bilham et al.* [1998] estimate an along-arc tensile strain rate in southern Tibet of 0.012 μstrain per year, corresponding to 12 mm/yr between SIMI and LHAS. Although this close agreement is an encouraging result, the current rate of extension between SIMI and TING (2±4 mm/yr) and SIMI and JOMO (3±2 mm/yr) is not significant, suggesting either that east-west extension is not uniformly distributed along the range or that the extension occurs only north of JOMO and TING.

The motion of LHAS is eastward in a Eurasian or southwest Tibetan reference frame (Figures 2 and 3), suggesting that east-west extension of southern Tibet accommodates eastward displacements rather than westward motion as suggested by *Molnar and Lyon-Caen* [1989]. LHAS is located south of the Beng Co and Jiali echelon segments of the right-lateral Karakorum-Jiali fault zone, which is thought to slip at about 15 mm/yr [*Armijo et al.*, 1989]. If so, central and northern Tibet would have to be moving eastward at an even higher rate between the left-lateral Altyn Tagh and Kunlun faults and the Karakorum-Jiali fault zone.

We can also examine the motion of SIMI, JOMO, TING, and LHAS with respect to the local plate convergence direction. The local direction of convergence

can be determined by subtracting the Eurasian and Indian predictions for each site (Table 2). Residual vectors can then be resolved into plate convergent and off-convergent directions. The off-convergent component of motion slowly increases as we move east from SIMI (1±2 mm/yr), JOMO (4±2 mm/yr), TING (5±4 mm/yr) to LHAS (13±3 mm/yr), with LHAS showing significant eastward divergence. We will need sites to the west of SIMI to test whether these sites show westward motion with respect to the local plate convergence direction.

King et al. [1997] find insignificant contraction across the Longmen Shan and 12–15±4 mm/yr strike slip on the left-lateral Xianshuihe-Xiaojiang fault. This result suggests that eastward displacement of southern and central Tibet is partially accommodated by southeast directed corner flow or clockwise rotation around the eastern syntaxis of the collision zone (Figure 7), as suggested by *Royden et al.* [1997] and *King et al.* [1997]. Eurasia-fixed velocities of sites on either side of the Xianshuihe fault shown in Figure 7 are dependent on the premise that there is insignificant strain between either SHAO or TAIW and *King et al.*'s [1997] GPS reference station at Chengdu, which is located east of the Xianshuihe fault and the Longmen Shan. Neither geologic nor seismic studies find evidence for significant strain across the South China block [*England and Molnar*, 1997b; *Holt et al.*, 1995]

The lack of shortening across the Longmen Shan [*King et al.*, 1997] and the ~10 mm/yr eastward motion of SHAO, TAIW, and a site in Korea relative to Eurasia [*Kato et al.*, 1998] suggest that coherent eastward displacement of Tibet and south China amounts to about 10 mm/yr (Figure 7). It has to be pointed out, however, that the eastern sites could possibly be affected by subduction and continental collision processes to the east. Continuously operating GPS sites at Wuhan and X'ian located well west of SHAO [*Kato et al.*, 1998] will soon provide the constraints that are needed to test these patterns.

6. Conclusions

North-south contraction across the Nepal Himalaya occurs at a rate of 18±2 mm/yr, suggesting that about 20 mm/yr of strain is accumulating across the locked portion of the Himalayan thrust system south of the Greater Himalaya. Our three-dimensional model inversions show that the detachment fault is locked over ~140 km width along a 500 km reach of the Nepal Himalaya. Future $M8$ earthquakes will eventually relieve the accumulating slip deficit. Of particular concern is the region between the 1905 Kangra and 1934 Bihar earthquake ruptures that may have built up as much as 6–15 m of slip potential. Our models suggest that significant differences in the active displacement patterns between west and east Nepal can be explained by a major structural segment boundary near 83° longitude, east of which the detachment is located at a shallower depth. A change in strike of a lineament of small to moderate earthquakes along the Himalaya and the inferred western edge of the 1934 Bihar earthquake rupture coincide with this possible segment boundary. However, models that attempt to account for the effects of viscous relaxation following the 1934 earthquake suggest that the differences could also be due to remnant postseismic deformation from that event.

We find east-west extension across southern Tibet at a rate of 11±3 mm/yr between northwestern Nepal and Lhasa. The spatial distribution of extension across Tibet is not well resolved by our data. However, extension is apparently occurring north of the strain accumulation zone of the Himalayan detachment system. The observed motion of Lhasa suggests that portions of southern Tibet displace eastward ahead of the Indian indenter and that some north-south shortening occurs across southern Tibet. If the east-west striking, right-lateral Karakorum-Jiali fault zone north of Lhasa slips at rates suggested by geologic estimates, then eastern central Tibet south of the Kunlun fault zone may move at 20 mm/yr to the east. Results from *King et al.* [1997] suggest that about half the eastward motion of Tibet is transferred south of the south China block toward Indochina by the southeast striking, left-lateral Xianshuihe-Xiaojiang fault zone. Eastward motions of about 10 mm/yr of sites in Shanghai and western Taiwan and the lack of discernible shortening across the Longmen Shan [*King et al.*, 1997] and the south China block suggest regional eastward displacement of Tibet and south China away from the collision zone. No significant strain is observed north of the Tien Shan and Mongolia.

We have successfully determined the pattern and mechanism of strain accumulation across the Nepal Himalaya and have provided some additional constraints on motions in southern Tibet and South China and the total width of the collision zone. Much controversy still focuses on the contributions of crustal thickening and extension, strike-slip faulting and eastward extrusion, as well as crustal block rotations in the accommodation of continental collision between India and Eurasia [*Molnar and Deng*, 1984; *England and Molnar*, 1997a; 1997b; *Avouac and Tapponnier*, 1993; *Peltzer and Saucier*, 1996; *Davy and Cobbold*, 1988; *England and Houseman*, 1986; *Peltzer et al.*, 1989]. GPS data are particularly suitable for resolving the active three-dimensional kinematics in a global reference frame. Ongoing and future GPS studies will provide answers to many of the outstanding questions pertaining to the geodynamics of this collision zone.

Acknowledgments. We would like to thank the IGS and their many support personnel for providing outstanding GPS data and data products. We also thank P. Athans, J. Avouac, R. Bendick, W. Berg, M. Bhatterrai, F. Blume, P. Bodin, V. Gaur, M. Jackson, S. Jade, D. Mencin, P. Molnar, P. Oli, B. O'Niell, M.R. Pandey, J. Paul, G. Rosborough, B.

Shrestha, F. Sigmundsson, B. Stephens, W. Wang, B. Washburn, UNAVCO, and all the members of Project Idylhim for help in various parts of this project. Figures were produced using GMT [*Wessel and Smith*, 1995]. JPL provided the GIPSY software. This research was supported by NSF grants EAR 9506677 and EAR 9727652 and NASA grants NAG-1908 and NAG5-6147. Earthquake locations are from the Council of the National Seismic System (CNSS) worldwide earthquake catalog provided by the Northern California Earthquake Data Center (NCEDC). We are grateful to Jim Savage, Gilles Peltzer, and Bob King for careful reviews of the manuscript.

References

Abdrakhmatov, K., et al., Relatively recent construction of the Tien Shan inferred from GPS measurements of present-day crustal deformation rates, *Nature, 384*, 450–453, 1996.

Armijo, R., P. Tapponnier, J.L. Mercier, and H. Tonglin, Quaternary extension in southern Tibet: Field observations and tectonic implications, *J. Geophys. Res., 91*, 13,803–13,872, 1986.

Armijo, R., P. Tapponnier, and T. Han, Late Cenozoic right-lateral strike-slip faulting in southern Tibet, *J. Geophys. Res., 94*, 2787–2838, 1989.

Argus, D., and R. Gordon, No-net rotation model of current plate velocities incorporating plate motion model NUVEL-1, *Geophys. Res. Lett., 18*, 2039–2042, 1991.

Arnadottir, T., and P. Segall, The 1989 Loma Prieta earthquake imaged from inversion of geodetic data, *J. Geophys. Res., 99*, 21,835–21,855, 1994.

Avouac, J.-P., and P. Tapponnier, Kinematic model of active deformation in Asia, *Geophys. Res. Lett., 20*, 895–898, 1993.

Baranowski, J., J. Armbruster, L. Seeber, and P. Molnar, Focal depths and fault plane solutions of earthquakes and active tectonics of the Himalaya, *J. Geophys. Res., 89*, 6918–6928, 1984.

Bilham, R., Location and magnitude of the 1833 Nepal earthquake and its relation to the rupture zones of contiguous great Himalayan earthquakes, *Curr. Sci., 69*, 101–128, 1995.

Bilham, R., P. Bodin, and M. Jackson, Entertaining a great earthquake in western Nepal: Historic inactivity and geodetic tests for the development of strain, *J. Nepal Geol. Soc., 11*, 73–88, 1995.

Bilham, R., K. Larson, J. Freymueller, and Project Idylhim Members, GPS measurements of present day convergence rates in the Nepal Himalaya, *Nature, 336*, 61–64, 1997.

Bilham, R., F. Blume, R. Bendick, and V.K. Gaur, Geodetic constraints on the translation and deformation of India: Implications for future great Himalayan earthquakes, *Curr. Sci., 74*, 213–229, 1998.

Boucher, C., Z. Altamimi, M. Feissel, and P. Sillard, Results and analysis of the ITRF 94, *IERS Tech. Note 20*, Int. Earth Rotation Serv. Cent. Bur., Obs. de Paris, Paris, 1996.

Burchfiel, C., Z. Chen, Y. Liu, and L. Royden, Tectonics of the Longmen Shan and adjacent regions, Central China, *Int. Geol. Rev., 37*, 661–735, 1996.

Bürgmann, R., K.M. Larson, and R. Bilham, Model inversion of GPS and leveling measurements across the Himalaya: Implications for earthquake hazards and future geodetic networks, Conference Paper for the Indo-US Workshop on Paleoseismicity, Dehra Dun, India, Wadia Inst. of Himalayan Geol., March 26–28, 1997.

Burtman, V.S., S. F. Skobelev, and P. Molnar, Late Cenozoic slip on the Talas-Ferghana fault, the Tien Shan, central Asia, *Geol. Soc. Am. Bull., 108*, 1004–1021, 1996.

Davy, P. and P. Cobbold, Indentation tectonics in nature and experiment, 1, Experiments scaled for gravity, *Bull. Geol. Inst. Uppsala, 14*, 129–141, 1988.

DeMets, C., R. Gordon, D. Argus, and S. Stein, Current plate motions, *Geophys. J. Int., 101*, 425–478, 1990.

DeMets, C., R. Gordon, D. Argus, and S. Stein, Effect of recent revisions to the geomagnetic reversal time scale on estimates of current plate motions, *Geophys. Res. Lett., 21*, 2191–2194, 1994.

England, P.C., and G.A. Houseman, Finite strain calculation of continental deformation, 2, Comparison with the India-Asia collision zone, *J. Geophys. Res., 91*, 3664–3676, 1986.

England, P.C., and P. Molnar, Active deformation of Asia: From kinematics to dynamics, *Science, 278*, 647–650, 1997a.

England, P.C., and P. Molnar, The field of crustal velocity in Asia calculated from Quaternary rates of slip on faults, *Geophys. J. Int., 130*, 551–582, 1997b.

Freymueller, J., R. Bilham, R. Bürgmann, K.M. Larson, J. Paul, S. Jade, and V. Gaur, Global Positioning System measurements of Indian plate motion and convergence across the lesser Himalaya, *Geophys. Res. Lett., 23*, 3107–3110, 1996.

Harrison, T.M., F.J. Ryerson, P. Le Fort, A. Yin, O.M. Lovera, and E.J. Catlos, A late Miocene-Pliocene origin for the Central Himalayan inverted metamorphism, *Earth Planet Sci. Lett., 146*, E1–E7, 1997.

Heki, K., Horizontal and vertical crustal movements from three-dimensional very long baseline interferometry kinematic reference frame: Implication for the reversal timescale revision, *J. Geophys. Res., 101*, 3187–3198, 1996.

Holt, W.E., M. Li, and A.J. Haines, Earthquake strain rates and instantaneous relative motions within central and eastern Asia, *Geophys. J. Int., 122*, 569–593, 1995.

Houseman, G.A., and P.C. England, Crustal thickening versus lateral expulsion in the India-Asia continental collision, *J. Geophys. Res., 98*, 12,233–12,249, 1993.

Jackson, M., and R. Bilham, Constraints on Himalayan Deformation inferred from vertical velocity fields in Nepal and Tibet, *J. Geophys. Res., 99*, 13,897–13912, 1994.

Kato, T., et al., Initial results from WING, the continuous GPS network in the western Pacific area, *Geophys. Res. Lett., 25*, 369–372, 1998.

Khattri, K.N., Great earthquakes, seismicity gaps, and potential for earthquake disaster along the Himalaya plate boundary, *Tectonophysics, 138*, 79–92, 1987.

King, R.W., F. Shen, B. C. Burchfiel, L. Royden, E. Wang, Z. Chen, Y. Liu, X. Zhang, J. Zhao, and Y. Li , Geodetic measurement of crustal motion in southwest China, *Geology, 25*, 179–182, 1997.

Kirby, S.H., Rock mechanics observations pertinent to the rheology of the continental lithosphere and the localization of strain along shear zones, *Tectonophysics, 119*, 1–27, 1985.

Larson, K.M., J. Freymueller, and S. Philipsen, Global plate velocities from the Global Positioning System, *J. Geophys. Res., 102*, 9961–9982, 1997.

Lichten, S., and J. Border, Strategies for high-precision GPS orbit determination, *J. Geophys. Res., 92*, 12,751–12,762, 1987.

Makovsky, Y., S. Klemperer, L. Huang, and D. Lu, Structural elements of the southern Tethyan Himalaya crust from wide-angle seismic data, *Tectonics, 15*, 997–1005, 1996.

Michel, G., C. Reigber, D. Angermann, J. Klotz, CATS Team, and GEODYSSEA Team, Ongoing and recent de-

formation in central and SE Asia (abstract), *Eos Trans. AGU, 78(46)* Fall Meet. Suppl., F172, 1997.

Molnar, P., Structure and tectonics of the Himalaya: Constraints and implications of geophysical data, *Annu. Rev. Earth Planet. Sci., 12*, 489–518, 1984.

Molnar, P., Inversion of profiles of uplift rates for the geometry of dip-slip faults at depth, with examples from the Alps and Himalaya, *Ann. Geophys., 5*, 663–670, 1987.

Molnar, P., A review of the seismicity and the rates of active underthrusting and the deformation of the Himalaya, *J. Himalayan Geol., 1*, 131–154, 1990.

Molnar, P., and Q. Deng, Faulting associated with large earthquakes and the average rate of deformation in central and eastern Asia, *J. Geophys. Res., 89*, 6203–6228, 1984.

Molnar P., and J. Gipson, A bound on the rheology of continental lithosphere using very long baseline interferometry: The velocity of south China with respect to Eurasia, *J. Geophys. Res., 101*, 545–553, 1996.

Molnar, P., and H. Lyon-Caen, Fault plane solutions of earthquakes and active tectonics of the Tibetan plateau and its margins, *Geophys. J. Int., 99*, 123–153, 1989.

Molnar, P., and P. Tapponnier, Cenozoic tectonics of Asia: Effects of a continental collision, *Science, 189*, 419–426, 1975.

Molnar, P., B. C. Burchfiel, L. K'unangyi, and Z. Ziyun, Geomorphic evidence for active faulting in the Altyn Tagh and northern Tibet and qualitative estimates of its contribution to the convergence of India and Eurasia, *Geology, 15*, 249–253, 1987.

Ni, J., and M. Barazangi, Seimotectonics of the Himalayan collision zone: Geometry of the underthrusting Indian plate beneath the Himalaya, *J. Geophys. Res., 89*, 1147–1163, 1984.

Okada, Y., Surface deformation due to shear and tensile faults in a half-space, *Bull. Seismol. Soc. Am., 75*, 1135–1154, 1985.

Pandey, M.R., R. P. Tandukar, J. P. Avouac, J. Lavé, and J. P. Masot, Interseismic strain accumulation on the Himalayan crustal ramp (Nepal), *Geophys. Res. Lett., 22*, 751–754, 1995.

Paul, J., et al., Microstrain stability of Peninsular India, 1864–1994, *Proc. Indian Acad. Sci. Earth Planet. Sci., 104*, 131–146, 1995.

Peltzer, G., and F. Saucier, Present day kinematics of Asia derived from geologic fault rates, *J. Geophys. Res., 101*, 27,943–27,956, 1996.

Peltzer, G., P. Tapponnier, and R. Armijo, Magnitude of late Quaternary left lateral displacements along the north edge of Tibet, *Science, 246*, 1285–1289, 1989.

Pollitz, F.F., Gravitational viscoelastic postseismic relaxation on a layered spherical Earth, *J. Geophys. Res., 102*, 17,921–17,941, 1997.

Ramsay, J.G., Shear zone geometry: A review, *J. Struct. Geol., 2*, 83–89, 1980.

Royden, L.H., B.C. Burchfiel, R.W. King, E. Wang, Z. Chen, F. Shen, and Y. Liu, Surface deformation and lower crustal flow in eastern Tibet, *Science, 276*, 788–790, 1997.

Savage, J.C., A dislocation model of strain accumulation and release at a subduction zone, *J. Geophys. Res., 88*, 4984–4996, 1983.

Savage, J.C., Comment on "The stress state implied by dislocation models of subduction deformation," *Geophys. Res. Lett., 23*, 2709–2710, 1996.

Savage, J.C., Displacement field for an edge dislocation in a layered half-space, *J. Geophys. Res., 103*, 2439–2446, 1998.

Seeber, L., and V. Gornitz, River profiles along the Himalayan arc as indicators of active tectonics, *Tectonophysics, 92*, 335–367, 1983.

Tandukar, R.P., et al., Microseismic epicentre map of Nepal Himalaya and adjoining region, scale 1:2,000,000, Nat. Seismol. Cent., Dep. of Mines and Geol., Kathmandu, Nepal, 1997.

Thatcher, W., Cyclic deformation related to great earthquakes at plate boundaries, *Bull. R. Soc. N.Z., 24*, 245-272, 1986.

Upreti, B.N., Stratigraphy of the western Nepal, Lesser Himalaya: A synthesis, *J. Nepal Geol. Soc., 13*, 11–28, 1996.

Wessel, P. and W. Smith, New version of the Generic Mapping Tools released, *Eos Trans. AGU, 76*, 329, 1995.

Zhao, W., et al., Deep seismic reflection evidence for continental underthrusting beneath southern Tibet, *Nature, 366*, 557–559, 1993.

Zoback, M.L., First and second-order patterns of stress in the lithosphere: The World Stress Map Project, *J. Geophys. Res. 97*, 11,703–11,728, 1992.

R. Bilham, Department of Geological Sciences and CIRES, University of Colorado, Boulder, CO 80309. (bilham@stripe.colorado.edu)

R. Bürgmann, Department of Geology and Geophysics, Univeristy of California, Berkeley, CA 94720. (burgmann@seismo.berkeley.edu)

J. T. Freymueller, Geophysical Institute, University of Alaska, Fairbanks, AK 99775. (jeff@giseis.alaska.edu)

K. M. Larson, Department of Geophysics, Stanford University, Stanford, CA 94305.

(Received April 24, 1998; revised August 17, 1998; accepted September 23, 1998.)